Volume 26
Number 26
14 July 2024
Pages 3433–3594

CrystEngComm

rsc.li/crystengcomm

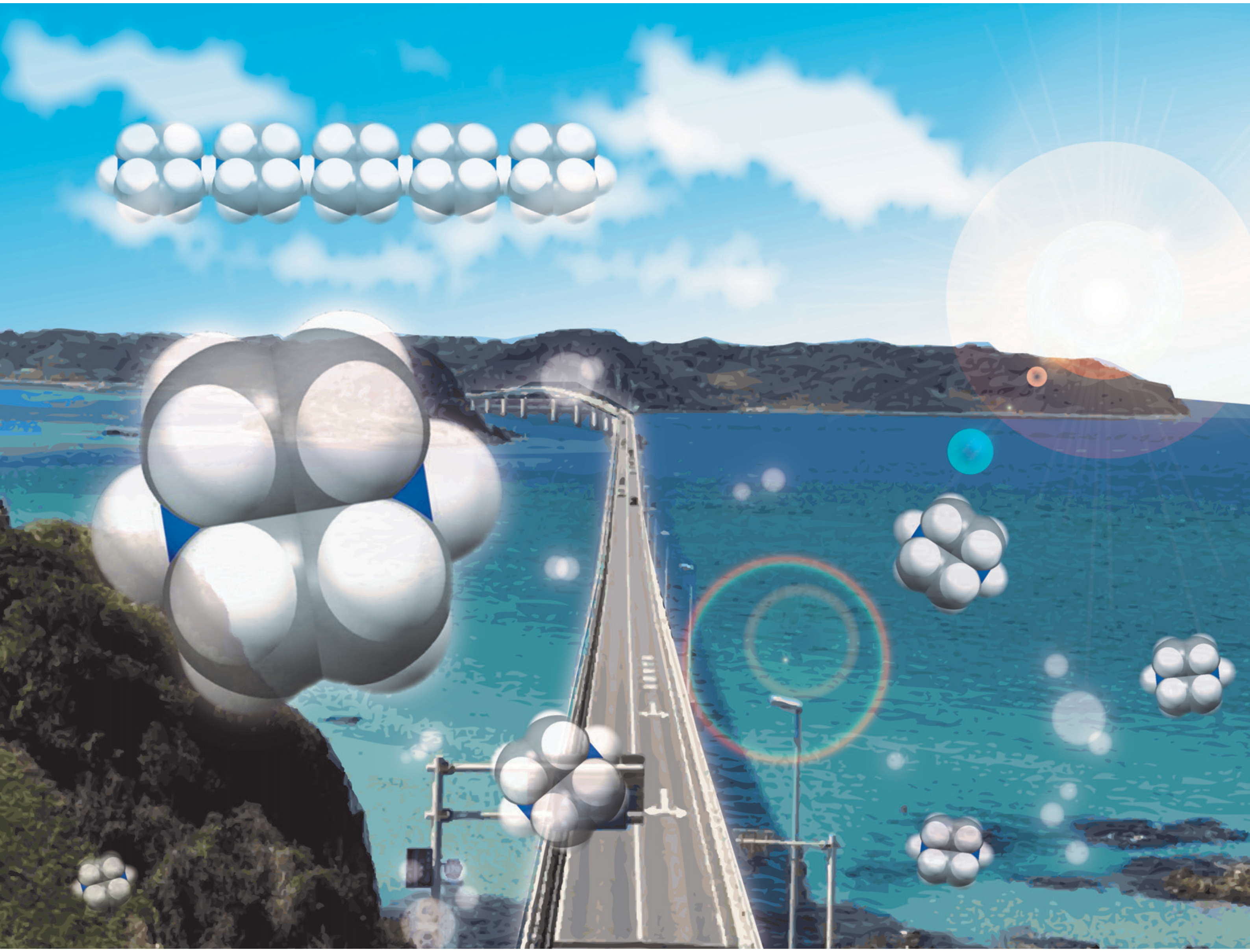

ISSN 1466-8033

ROYAL SOCIETY
OF **CHEMISTRY**

PAPER
Ryo Tsunashima *et al.*
Effect of halide solid solution on the structure, phase transition behaviour and dielectric properties of dabcoH$^+$ chains

CrystEngComm

ROYAL SOCIETY OF CHEMISTRY

PAPER

Cite this: *CrystEngComm*, 2024, **26**, 3468

Effect of halide solid solution on the structure, phase transition behaviour and dielectric properties of dabcoH$^+$ chains†

Yuki Ohishi,[a] Kohei Sambe,[b] Shun Dekura,[bc] Tomoyuki Akutagawa,[bc] Atsuko Masuya-Suzuki[ad] and Ryo Tsunashima*[ad]

1,4-Diazabicyclo[2.2.2]octane (dabco) forms one-dimensional chains through intermolecular N–H$^+$⋯N hydrogen bonds and exhibits ferroelectricity originating from proton transfer. The size of the polarized domain differs depending on the size, symmetry, and polarizability of the counter anions. Herein, two binary halide solid solutions of dabcoHBr mixed with dabcoHCl (**ClBr**) and dabcoHI (**BrI**) were prepared, and the temperature dependence of the single crystal structure and the phase transition behaviour were investigated. The solid solution of **ClBr** contained 3% Cl$^-$ in dabcoHBr; thus, the lattice length, space group, and volume were similar to those of dabcHBr. The phase transition temperature from the hydrogen-bonded structure to the ion-pair structure decreased from 458 to 440 K upon mixing with Cl$^-$. In contrast, solid solution **BrI** was formed with all proportional solid solutions, and the crystallographic parameters characterised by single-crystal X-ray diffraction (XRD) analysis obeyed Vegard's law. Phase transition behaviours were investigated for single crystals of Br : I = 8 : 2 (**Br$_{0.80}$I$_{0.20}$**) *via* temperature-variable single crystal XRD analysis. A new structural range was observed between 251–373 K. Within this range, the intermolecular N–H$^+$⋯N hydrogen bonds were weakened. This was also a ferroelectric phase similar to that of the original dabcoHBr. In the high-temperature range, a phase transition from the hydrogen-bonded phase to the ion-pair phase was observed at 435 K, which was lower than the 458 K of dabcoHBr.

Received 29th March 2024,
Accepted 7th June 2024

DOI: 10.1039/d4ce00310a

rsc.li/crystengcomm

Introductions

The characteristics of ferroelectric materials, which include piezoelectric, pyroelectric, and nonlinear optical properties, facilitate their application in memory, capacitors, and thermal sensors.[1–3] However, metal-containing ferroelectrics often include metals that are harmful to the environment and human health, such as lead zirconate titanate (PZT) and barium titanate (BTO). Macroscopic ferroelectrics originate from a uniform arrangement of dipole moments. Conversely, relaxor ferroelectrics are another type of ferroelectric material that exhibits nanoscale domains. Polarized domains are formed at the mesoscopic scale and grow under an applied electric field.[4–8] They exhibit high dielectric and piezoelectric properties and broad temperature–frequency dispersions. These materials have been used in energy storage devices and piezoelectric actuators. Relaxor ferroelectrics are often observed in metal-containing perovskite-type composite oxides with an A(BB′)O$_3$ chemical formula, where A, B and B′ are Pb, low valence state metal ions and d$_0$ transition metal, respectively.[9–12] Therefore, an understanding of metal-containing relaxor ferroelectrics is being developed with design guidelines based on the characteristics of metals.

Metal-free ferroelectrics composed of organic molecules and/or halides are lightweight, safer for humans and the environment, and easily processed.[13–18] The mechanism of ferroelectricity in metal-free ferroelectrics differs from the displacement of atoms from centrosymmetric positions in metal-containing ferroelectrics. In contrast, metal-free ferroelectrics include orientational polarization of the molecules by inverting their orientation *via* an outer electric field and displacing the proton in the hydrogen bond at appropriate interatomic distances.

Several hydrogen-bonded ferroelectrics, such as dabcoHA (A = BF$_4^-$, ClO$_4^-$, ReO$_4^-$), dabco = 1,4-diazabicyclo[2.2.2]octane,[19–21] have been shown to exhibit large polarization comparable to

---

[a] *Graduate School of Sciences and Technology for Innovation, Yamaguchi University, Yoshida 1677-1, Yamaguchi, 753-8512, Japan. E-mail: ryotsuna@yamaguchi-u.ac.jp*

[b] *Graduate School of Engineering, Tohoku University, Sendai 980-8577, Japan*

[c] *Institute of Multidisciplinary Research for Advanced Materials (IMRAM), Tohoku University, Sendai 980-8577, Japan*

[d] *Chemistry Course, Faculty of Science, Yamaguchi University, Yoshida 1677-1, Yamaguchi, Japan*

† Electronic supplementary information (ESI) available: Details on experimental procedures, DFT and crystallographic analysis. CCDC 2340566–2340574. For ESI and crystallographic data in CIF or other electronic format see DOI: **https://doi.org/10.1039/d4ce00310a**

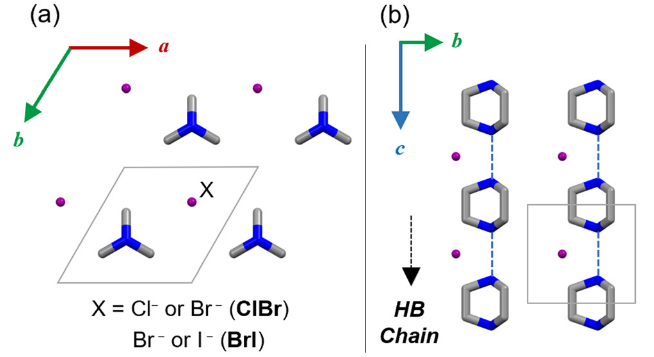

Fig. 1 Crystal structure of dabcoHX in (a) *ab* and (b) *bc* planes (C: grey, N: blue and halides X: purple). H atoms are omitted for clarity.

those of metal-containing ferroelectrics at room temperature.[22–27] The counter anions, A^-, are distributed within the space of the hydrogen-bonded dabcoH^+ chains and bridging them (Fig. 1). The proton transfer in hydrogen bonding, as well as the orientation and ionic polarization of A^- are components of the ferroelectric mechanism. DabcoHX (X = Br^-, I^-) contains spherical anions and exhibits a different polarization order to that of dabcoHA.[28,29] Dabco forms a one-dimensional chain; however, its order is short-ranged and formed with weak electronic polarizations of anions. Therefore, dabcoHX is a relaxor ferroelectric with proton transfer.[28–30] Mono-salts consisting of dabcoH^+ form a polarization order owing to the size, polarizability, and symmetry of the anion.

Solid solutions are formed by the homogeneous mixing of two or more components to produce a single solid phase, such as the relaxor ferroelectrics of $A(BB')O_3$ previously described. The Curie temperature, polarization, and dielectric constant of a metal-containing solid solution are controlled by its composition. In addition, a morphotropic phase boundary (MPB) is observed when crystals with different symmetries are used in solid solutions. Physical properties such as the dielectric and piezoelectric constants exhibited anomalous behaviour at the MPB.[31–34]

Solid solutions of molecular crystals are often substitutional solid solutions of isomorphic structures, for example, replaced by a molecule with the same family of elements. The phase transition behaviour and molecular motility in the crystals are less dependent on the composition. However, there are examples of molecular crystalline solid solutions whose phase transition behaviours and molecular mobilities are composition-dependent;[35–39] for example, solid solutions partially substituted with different halogens. CM (cyclohexylmethylammonium) salts undergo a phase transition at a temperature that depends on composition.[40] Furthermore, a previous study showed high piezoelectricity with $(TMFM)_x(TMCM)_{1-x}CdCl_3$ (TMFM = trimethylfluoromethyl ammonium, TMCM = trimethylchloromethyl ammonium).[41]

Differently from the inorganic relaxor, solid solution of the molecular-based metal-free relaxor has not been developed yet. This study focuses on the structure and phase transition behaviour of halide solid solutions of dabcoH^+ salts. The inorganic relaxer ferroelectrics have developed with solid solutions of varieties of metals. However, molecular crystals often lack diversity in structure and properties. This arises from the fact that molecular solid solution is obtained from isostructural pares whose structure and properties are similar.[36] In this study, we succeeded in crystallizing the halide solid solution of the dabco-based metal-free relaxer and unveiled composition dependence on the structures, phase transition behaviours, and ferroelectricity.

Results and discussion

Preparation and composition determination of solid solutions ClBr and BrI

The isolation of crystallised dabcoHX from an aqueous solution of a 1 : 1 mixture of dabco with acid HX has been demonstrated.[28] This was followed by the experimental procedures for **ClBr** and **BrI**, wherein acids HBr and HX (HX = HCl or HI) were mixed at a ratio of x' which is the experimental mixing ratio of HBr to HI. Good-quality single crystals suitable for single-crystal XRD environments were isolated after slow solvent evaporation by keeping the solution in the atmosphere for several days. Furthermore, scanning electron microscopy-energy dispersive X-ray spectroscopy (SEM-EDS) mapping showed the uniform dispersion of both halogens within the crystal (Fig. S1†).

The solid solution ratio of the halide ions was estimated using elemental analysis of carbon, hydrogen, and nitrogen (CHN). The relationship between the experimental mixing ratio, x', and the solid solution ratio determined experimentally, x, is shown in Fig. 2. Regarding the solid solution **ClBr**, no proportional relationship was observed between them. In solid solution **ClBr** with a high composition of Cl^-, the concentration of Br^- was approximately 7% (referred to as $\mathbf{Cl_{0.93}Br_{0.07}}$). Contrary to Cl^- rich **ClBr**, Cl^- in **ClBr** with a high composition of Br^- was approximately 3% (referred to as $\mathbf{Cl_{0.03}Br_{0.97}}$). The low miscibility of Cl^- and Br^- occurs because of the differences between the structure of the end-members. DabcoH^+ interacts with Cl^- in the crystal of dabcoHCl to produce an ion-pairing structure.[42] A hydrogen-bonded chain structure is observed in dabcoHCl trihydrate.[42] The PXRD diffraction pattern of the $\mathbf{Cl_{0.93}Br_{0.07}}$ solid solution corresponded to that of $(dabcoHCl)\cdot 3H_2O$. Conversely, the $\mathbf{Cl_{0.03}Br_{0.97}}$ corresponded to the diffraction pattern of dabcoHBr consisting of hydrogen-bonded chains (Fig. S2†).

A linear relationship was observed between the mixing ratio of the solid solution **BrI** and the composition ratio of the crystal. The components were mixed at all proportions, which is typical for all proportional solid solutions. **BrI** is highly miscible because of the isomorphism of dabcoHBr and dabcoHI.

Crystallographic study and phase transition behaviour of ClBr

Single crystals of the solid solution $\mathbf{Cl_{0.03}Br_{0.97}}$ were isolated for SC-XRD at 298 K. $\mathbf{Cl_{0.03}Br_{0.97}}$ was crystallised with space group $P\bar{6}m2$, which was the same as that of dabcoHBr (Fig.

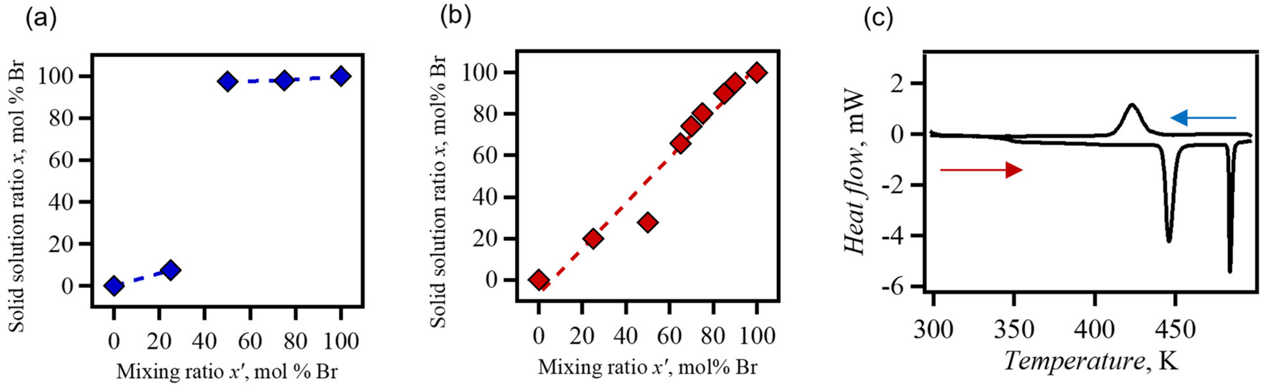

Fig. 2 Plot of the experimental mixing ratio (x') (horizontal axis) *versus* the solid solution ratio (x) (vertical axis) calculated by elemental analysis for (a) solid solution **ClBr** and (b) solid solution **BrI**. (c) DSC of solid solution $\mathbf{Cl_{0.03}Br_{0.97}}$. Measurements were conducted between 273–500 K, at a sweep rate of 10 K $\mathrm{min^{-1}}$ and under N_2 atmosphere.

S3†). The lattice constants, *a* and *c*, and lattice volume were 6.6645(5), 5.3238(4) Å, and 204.78(3) $Å^3$, respectively. Therefore, the crystal structure of solid solution $\mathbf{Cl_{0.03}Br_{0.97}}$ was not significantly different from that of dabcoHBr[43] (6.6650(10), 5.3130(10) Å, and 204.40(6) $Å^3$).

DabcoHBr underwent a two-step phase transition when heated at 458 K and 471 K.[28] The first transition at 458 K corresponded to the breaking of hydrogen bonds; the $N–H^+\cdots N$ hydrogen-bonded chain structure (phase III) was transited to the ion-pair structure with $NH^+\cdots Br^-$ (phase II). At 471 K, another hydrogen bond was formed between the methylene moiety and bromide (phase I). The structural phase transition behaviour of $\mathbf{Cl_{0.03}Br_{0.97}}$ was investigated by differential scanning calorimetry (DSC) (Fig. 2(c)). The corresponding two-step phase transition was observed in the solid solution $\mathbf{Cl_{0.03}Br_{0.97}}$, whereas phase transition temperature from phase III to phase II was decreased to 440 K from 458 K for dabcoHBr, indicating decreases in transition enthalpy (ΔH). According to the relationship $\Delta H = T\Delta S$ for a phase transition, and given that the transition entropy (ΔS) is comparable to dabcoHBr and $\mathbf{Cl_{0.03}Br_{0.97}}$, ΔH is expected to decrease with addition of Cl^-. The estimated ΔH was 4.6 kJ $\mathrm{mol^{-1}}$, a slight decrease from 5.1 kJ $\mathrm{mol^{-1}}$ for dabcoHBr.[28]

The subsequent heating of the ion-pair phase II resulted in a further transition at 481 K; ΔH and ΔS were 3.5 kJ $\mathrm{mol^{-1}}$ and 7.2 J $\mathrm{mol^{-1}\ K^{-1}}$, respectively. Whereas, the cooling process exhibited a thermal anomaly characterized by a single-step broad peak at 438 K with ΔH = 3.7 kJ $\mathrm{mol^{-1}}$, which is lower than the sum of ΔH for heating process. PXRD pattern at 298 K after heating at 500 K was identical to that of phase III, indicating a reversible phase transition process between hydrogen bonding phase and ion-pair phase (Fig. S4†). It was suggested that the decrease in ΔH is due to a phase transition, which involves a gradual change in structure, such as a second-order type phase transition.

Crystallographic study of BrI

The high quality of BrI solid solution crystals allowed for SC-XRD analysis across all compositions. The temperature and composition dependence of the structure were evaluated between 112–373 K. The crystallographic data of x = 0.19, 0.27, 0.64, 0.74, 0.80, 0.90 and 0.95 at 298 K are summarised in Table 1. The crystal structures of the solid solutions with all compositions were isomorphic to dabcoHBr and dabcoHI. The Br-to-I ratio estimated from the occupancy, which was optimised by crystallographic analysis, showed good agreement with the ratio obtained from elemental analysis (Table S1†).

Fig. 3(a) shows a plot of the *a*-axis length (⊥ hydrogen bonding) and *c*-axis length (// hydrogen bonding) *versus* composition. In dabcoHBr and dabcoHI, the difference in the ionic radii of the counter anions ware appeared in those of *a*-axis lengths, which corresponded to the distance between the hydrogen-bonded chains. The dependence of the *a*- and *c*-axis lengths on composition was linear and followed Vegard's law.

Both of dabcoHBr and $\mathbf{Br_{0.80}I_{0.20}}$ had distribution in crystallographic data (Fig. 3(b and c)). For dabcoHBr, the 2σ ranges (97%) for the lattice lengths *a* and *c* were 6.6323–6.6975 and 5.2846–5.3454, respectively. Those of $\mathbf{Br_{0.80}I_{0.20}}$ were comparable; 6.7151–6.7495 and 5.3184–5.3308. Thus, distribution observed in $\mathbf{Br_{0.80}I_{0.20}}$ is not originated from heterogeneousity in ratio of Br^- and I^-, rather intrinsic differences. A single crystal of $\mathbf{Br_{0.80}I_{0.20}}$ which has the largest *a*-axis (entry 15) was used to evaluate temperature-dependence between 112–373 K (Table S3†).

The temperature dependence of the lattice constant of the end-member dabcoHBr was reported by Szafrański *et al.*[28] The *a*- and *c*-axis lengths exhibited a linear increase as the temperature increased from 95 to 400 K (phase III). However, the temperature dependence of the lattice length in $\mathbf{Br_{0.80}I_{0.20}}$ changed at ∼250 K for the *a*- and *c*-axes (Fig. S6†), indicating that phase III in dabcoHBr was divided into two ranges—the low-temperature range (LTR; ≤250 K) and the medium-temperature range (MTR; 251–373 K). Table 2 lists the coefficients of thermal expansion, β, calculated using the formula: $\alpha = \alpha_0(1 + \beta T)$. The β values in dabcoHBr were constant at the *a*-axis ($4.46 \times 10^{-5}\ \mathrm{K^{-1}}$) and the *c*-axis (1.78 ×

10^{-5} K^{-1}). However, increasing the temperature from LTR to MTR in **Br**$_{0.80}$**I**$_{0.20}$ increased the β values on the *a*- and *c*-axes by 1.6- and 2.2-fold, respectively. The temperature dependence of the lattice volume *V* corresponded to the lattice length.

The temperature dependence of the N···N distance between dabco molecules was investigated to determine the details of the hydrogen bonds (Fig. S7†). The N···N distance in dabcoHBr increased linearly with temperature, reaching 2.787(8) Å at 293 K in phase III.[44] The N···N distance in **Br**$_{0.80}$**I**$_{0.20}$ remained constant at 2.78(2) Å in LTR which corresponds to that of dabcoHBr. At 251 K the N···N distance began to increase but subsequently became constant at ~2.81 Å at 298–373 K. The elongation of the N···N distance to MTR resulted in weaker hydrogen bonding at MTR compared to LTR, which affected proton motility in hydrogen bonds. Using density functional theory (DFT), the activation barriers for proton motion at LTR (N···N distance: 2.78 Å) and MTR (N···N distance: 2.81 Å) were estimated as 0.30 and 0.37 eV, respectively (Fig. S8†).

Dielectric properties of solid solution Br$_{0.80}$I$_{0.20}$

The dabcoHBr exhibited a frequency–temperature-dependent dielectricaddition, a reduction in the dielectric anomaly in the *c*-axis direction between 180–300 K.[28] In solid solution **Br**$_{0.80}$**I**$_{0.20}$, the temperature dependence of the complex permittivity (120–370 K) was evaluated using single crystals along the *a*- and *c*-axis directions (Fig. 4). **Br**$_{0.80}$**I**$_{0.20}$ exhibited temperature- and frequency-independent dielectric anomalies along the *a*- and *c*-axes at ~250 K. This temperature was similar to that of the change from LTR to MTR. In addition, a reduction in the dielectric constant was observed along the *c*-axis when the temperature was above 250 K, which agreed with the increased activation energy of protons in the N···N hydrogen bond. *P–E* hysteresis measurements were performed in the *c*-axis direction at 298 K using single crystals (Fig. 5). The hysteresis loops indicated the ferroelectricity of MTR. However, the MTR is the non-polar space group *P*-6 *m*2 and there should be no spontaneous polarisation at *E* = 0. Previous studies have reported that dabcoHBr and dabcoHI are relaxor ferroelectrics that exhibit reversible pyroelectric current.[28,29] Hysteresis loops well-corresponds to that of relaxor ferroelectrics reported in inorganic relaxor ferroelectrics.[5,8]

Phase transition behaviour of solid solution Br$_{0.80}$I$_{0.20}$

The phase transition behaviour of **Br**$_{0.80}$**I**$_{0.20}$ was investigated DSC (Fig. 6). Endothermal peaks were observed in the DSC chart at 435 K and 464 K (ΔH = 5.36 and 3.18 kJ mol^{-1}, ΔS = 12.32 and 6.853 J mol^{-1} K^{-1}). The phase transition temperatures in **Br**$_{0.80}$**I**$_{0.20}$ decreased compared to those in dabcoHBr. The PXRD patterns measured at 480 K (Fig. S10†) were similar to those of phase I of dabcoHBr,[28] suggesting that **Br**$_{0.80}$**I**$_{0.20}$ also undergoes phase transitions from the hydrogen-bonded structure (phase III) to the ion-pair

Table 1 Crystallographic data for solid solution **BrI**

Compound	**Br**$_{0.19}$**I**$_{0.81}$	**Br**$_{0.27}$**I**$_{0.73}$	**Br**$_{0.64}$**I**$_{0.36}$	**Br**$_{0.74}$**I**$_{0.26}$	**Br**$_{0.80}$**I**$_{0.20}$	**Br**$_{0.90}$**I**$_{0.10}$	**Br**$_{0.95}$**I**$_{0.05}$
Formula	$C_6H_{13}N_2Br_{0.19}I_{0.81}$	$C_6H_{13}N_2Br_{0.27}I_{0.73}$	$C_6H_{13}N_2Br_{0.64}I_{0.36}$	$C_6H_{13}N_2Br_{0.74}I_{0.26}$	$C_6H_{13}N_2Br_{0.80}I_{0.20}$	$C_6H_{13}N_2Br_{0.90}I_{0.10}$	$C_6H_{13}N_2Br_{0.95}I_{0.05}$
Crystal system	Hexagonal						
Space group	$P\bar{6}m2$						
a, Å	7.0554(4)	6.9445(9)	6.8337(5)	6.8015(6)	6.7541(6)	6.6949(4)	6.6793(6)
c, Å	5.3473(3)	5.3334(5)	5.3349(3)	5.3298(4)	5.3383(4)	5.3265(4)	5.3178(5)
V, Å^3	230.54(3)	222.75(6)	215.76(3)	213.53(4)	210.90(4)	206.76(3)	205.46(4)
Z	1						
ρ_{calc}, g cm^{-3}	1.665	1.695	1.616	1.597	1.594	1.589	1.580
Reflections collected	1334	809	1547	803	1246	778	1234
Independent reflections	245	218	240	224	231	212	225
Data/restraints/parameters	245/0/11	218/0/11	240/0/12	224/0/11	231/0/12	212/0/11	225/0/11
Goodness of fit on F_2	1.097	1.081	1.077	1.206	1.114	1.240	1.080
Final *R* indices [$I \geq 2\sigma(I)$]	R_1 = 0.0141 wR_2 = 00353	R_1 = 0.0263 wR_2 = 0.0667	R_1 = 0.0525 wR_2 = 0.1272	R_1 = 0.0436 wR_2 = 0.1136	R_1 = 0.0389 wR_2 = 0.0930	R_1 = 0.0155 wR_2 = 0.0427	R_1 = 0.0314 wR_2 = 0.0717
Final *R* indices [all data]	R_1 = 0.0141 wR_2 = 0.0353	R_1 = 0.0263 wR_2 = 0.0667	R_1 = 0.0533 wR_2 = 0.1275	R_1 = 0.0436 wR_2 = 0.1136	R_1 = 0.0394 wR_2 = 0.0933	R_1 = 0.0155 wR_2 = 0.0427	R_1 = 0.0327 wR_2 = 0.0723
Temperature, K	298						

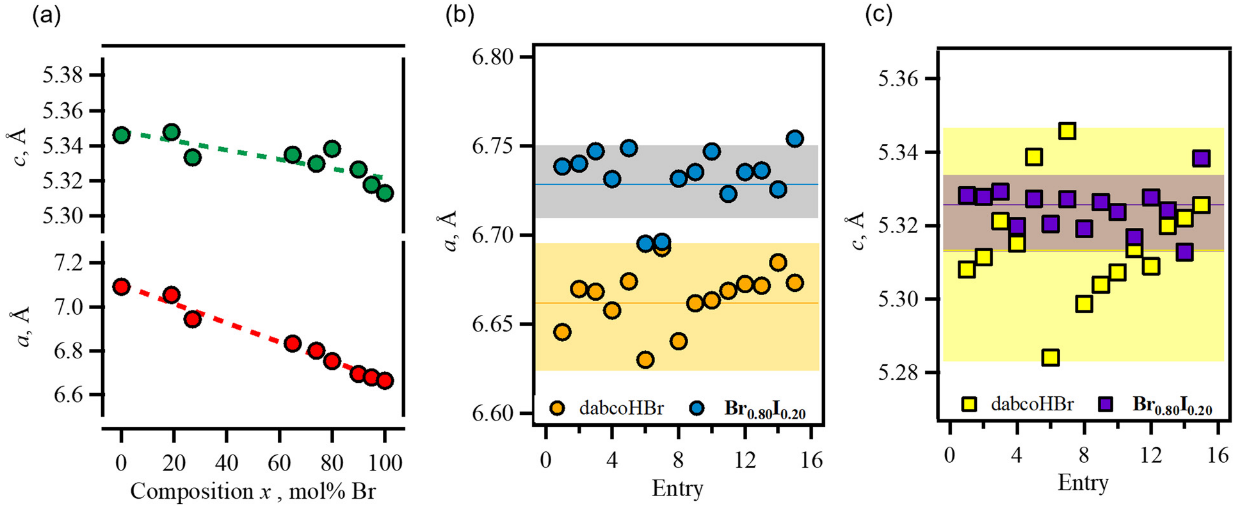

Fig. 3 (a) Composition dependence of lattice constants in solid solution **BrI**. (b and c) Dispersion of lattice constants in 15 single crystals of dabcoHBr and $\mathbf{Br_{0.80}I_{0.20}}$. The coloured areas depict average value ±2σ range. Lines indicate mean values. (b) *a*-axis. (c) *c*-axis.

structure of phase I *via* phase II. The decrease in phase transition temperature from phase III to phase II is consistent with the increase in N⋯N distance at MTR of $\mathbf{Br_{0.80}I_{0.20}}$ from dabcoHBr. During cooling process, an exothermal process was observed with a single peak at 319 K. The ΔH was estimated to be 8.30 kJ mol^{-1}, which agrees with the sum of heating process. This indicates that the phase transition is reversible but has a large thermal hysteresis.

The phase transition behaviour of $\mathbf{Br_{0.19}I_{0.81}}$ was investigated by DSC in order to investigate the lowest limit at which the compound undergoes a transition to the ion-pair phase (Fig. S11†). Endothermic peaks at 414 K and 434 K were observed during the heating process and an exothermic peak at 332 K during the cooling process. This behaviour was similar to that of $\mathbf{Br_{0.80}I_{0.20}}$. The PXRD pattern measured at 470 K (Fig. S12†) was similar to phase I of dabcoHBr,[28] suggesting that $\mathbf{Br_{0.19}I_{0.81}}$ also undergoes a phase transition to an ion-pair structure. A phase transition to an ion-pair structure was suggested for **BrI** at least up to a Br$^-$ concentration of 19%. Fig. S13† is DSC of other solid solutions. The corresponding phase transitions were observed with transition temperature decreased with content of sI$^-$ increases.

Conclusion

Two halide solid solutions (**ClBr** and **BrI**), which had one-dimensional hydrogen-bonded chain structures, were prepared in dabcoHX. Depending on the end-member structure, **ClBr** and **BrI** exhibited different miscibilities. $\mathbf{Cl_{0.03}Br_{0.97}}$ had a Cl$^-$ concentration of 3% and the lattice lengths were similar to those of dabcoHBr. Mixing Cl$^-$ reduced the temperature at which the phase transition from a hydrogen-bonded chain structure to an ion-pair structure occurred; the temperature of the transition for dabcoHBr changed from 458 K to 440 K. In contrast, **BrI** was all

Table 2 Coefficient of thermal expansion for each lattice constant in solid solution $\mathbf{Br_{0.80}I_{0.20}}$

	LTR	MTR
a, 10^{-5} K^{-1}	2.993	4.814
c, 10^{-5} K^{-1}	0.8285	1.822
V, 10^{-5} K^{-1}	6.864	12.40

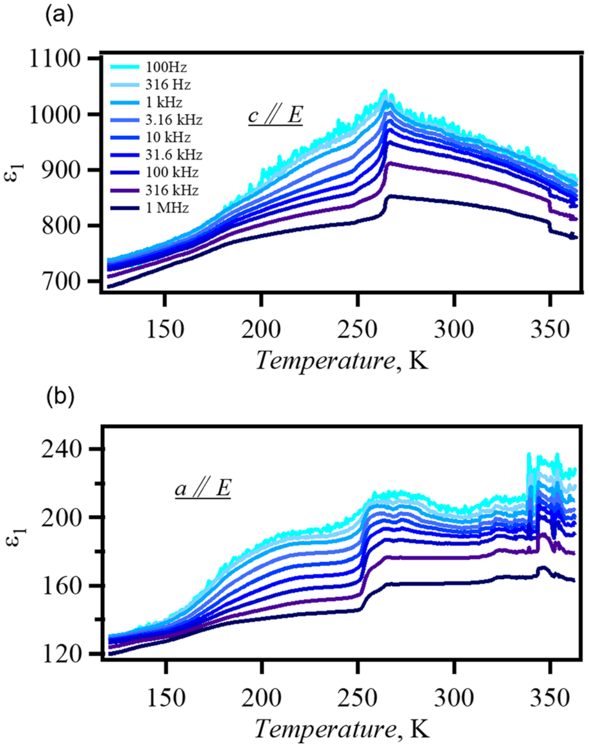

Fig. 4 (a and b) Temperature dependence of complex permittivity (a: *c*-axis direction, b: *a*-axis direction).

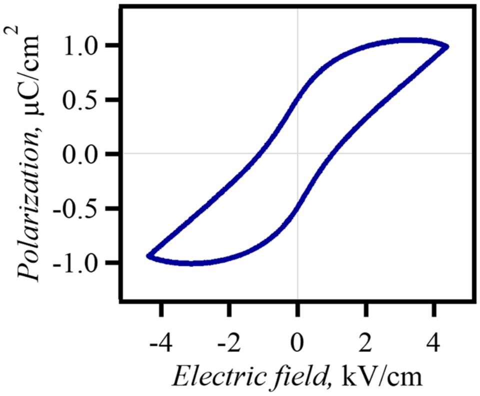

Fig. 5 *P–E* hysteresis loop of $\mathbf{Br_{0.80}I_{0.20}}$ measured at 298 K on the *c*-axis (20 Hz).

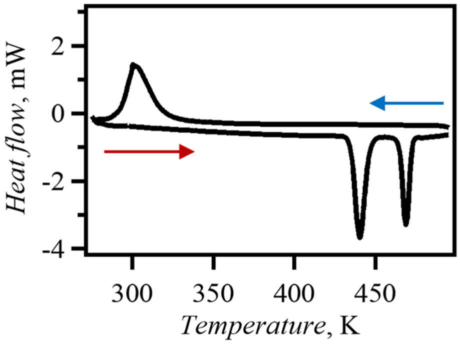

Fig. 6 Measurements were performed on $\mathbf{Br_{0.80}I_{0.20}}$ between 273–500 K, at a sweep rate of 10 K $\min^{-1}$ and under N_2 atmosphere.

proportional solid solution in which the lattice lengths and volume obeyed Vegard's law. A new structural range, MTR, was observed between 251–373 K in solid solution $\mathbf{Br_{0.80}I_{0.20}}$. Within this range, the hydrogen bonds were weakened. DFT analysis showed that change from LTR to MTR corresponded to a 0.07 eV increase in the activation energy of proton motility. These structural differences also appeared in the temperature dependence of complex permittivity. These results suggest that halide admixture can change the proton motility and the strength of hydrogen bonds, which are the mechanisms of dabco-based hydrogen bonding ferroelectric.

Experimental

Synthesis of solid solution ClBr and BrI

Commercially available dabco, HCl, HBr, and HI were used as received without further purification. A 10 mmol solution of dabco (1,4-diazabicyclo[2.2.2]octane) was mixed with an acid solution (HCl: 0.8 mL, HBr: 1.1 mL or HI: 1.4 mL) at a 1 : 1 molar ratio. Crystals were obtained by solvent evaporation under shaded light for several days. The solid solution **ClBr** was crystallised using the preparation ratio to HCl: $1 - x'$ and HBr: x' for each corresponding acid, $x' = 0$, 0.25, 0.50, 0.75, or 1 (yield 37.7, 35.5, 41.8, 44.6, and 46.5%). Solid solution **BrI** was crystallised using the same method as **ClBr**, with HBr: x', HI: $1 - x'$, and with preparation ratios of $x' = 0$, 0.25, 0.50, 0.65, 0.70, 0.75, 0.85, 0.90, or 1 (yield 42.6, 45.8, 35.2, 32.2, 31.4, 43.8, 37.5, 41.5, and 46.5%). For further details, see ESI.†

Measurement

XRD. Single-crystal X-ray structure analysis was performed using a Rigaku XtaLAB Synergy R, DW system, Hypix, with source: Mo Kα and processing software CrysAlisPro. Powder XRD at room temperature was performed using a Rigaku Mini Flex 600, whereas temperature-variable powder XRD was performed using a Rigaku Smart Lab, source: Cu Kα, under N_2 atmosphere.

SEM-EDS. Measurements were performed using a JEOL JSM-7600F instrument and an energy-dispersive X-ray generator. The measurements were performed after the carbon tape was stretched over the brass, a sample was placed on the tape, and gold was deposited using a vacuum evaporation system (Au, Sanyu).

DSC. Rigaku Thermo plus REVO2 Differential Scanning Calorimeter Measurements were conducted in an N_2 atmosphere at a sweep rate of 10 K $\min^{-1}$ using a DSCvesta instrument.

Complex permittivity. Measurements were made in the frequency range of 100–1 MHz using an E4980AL Precision LCR Meter (KEYSIGHT). The measurements were performed under vacuum, and the temperature was controlled using a LakeShore 335 Temperature Controller.

***P–E* hysteresis.** Measurements were performed using a RADIANT Precision LC II instrument.

DFT. Potential energy differences (ΔE) were calculated by a function of B3LYP/6-31G(d,p) using N⋯N distances obtained from the structural analysis. Gaussian software was used.

Conflicts of interest

There are no conflicts to declare.

Acknowledgements

The authors acknowledge financial support from the "Extensive contribution of structural sciences from leading-edge materials to cultural & archaeological works" by Yamaguchi University, JSPS KAKENHI (22H02054) and the Cooperative Research Program of the Network Joint Research Centre for Materials and Devices of Japan.

Notes and references

1 M. Acosta, N. Novak, V. Rojas, S. Patel, R. Vaish, J. Koruza, G. A. Rossetti, Jr. and J. Rodel, *Appl. Phys. Rev.*, 2017, **4**, 041305.
2 X. Wei, N. Domingo, Y. Sun, N. Balke, R. E. Dunin-Borkowski and J. Mayer, *Adv. Energy Mater.*, 2022, **12**, 2201199.
3 J. F. Scott and C. A. P. De Araujo, *Science*, 1989, **246**, 4936.

4 A. Kholkin, A. Morozovska, D. Kiselev, I. Bdikin, B. Rodriguez, P. Wu, A. Bokov, Z.-G. Ye, B. Dkhil, L.-Q. Chen, M. Kosec and S. V. Kalinin, *Adv. Funct. Mater.*, 2011, **21**, 1977–1987.

5 F. Li, S. Zhang, D. Damjanovic, L.-Q. Chen and T. R. Shrout, *Adv. Funct. Mater.*, 2018, **28**, 1801504.

6 H. Zhang, B. Yang, A. D. Fortes, H. Yan and I. Abrahams, *J. Mater. Chem. A*, 2020, **8**, 23965.

7 H. Pan, S. Lan, S. Xu, Q. Zhang, H. Yao, Y. Liu, F. Meng, E.-J. Guo, L. Gu, D. Yi, X. R. Wang, H. Huang, J. L. M. Driscoll, L.-Q. Chen, K.-J. Jin, C.-W. Nan and Y.-H. Lin, *Science*, 2021, **374**, 100–104.

8 S. Wang, F. Yan, J. Qian, G. Ge, Z. Fu, Z. Pan, F. Zhang, J. Lin, K. Zeng, C. Chen, B. Shen, Z. Liu and J. Zhai, *Energy Storage Mater.*, 2024, **66**, 103155.

9 I.-W. Chen, P. Li and Y. Wang, *J. Phys. Chem. Solids*, 1996, **57**, 1525–1536.

10 D. J. Goossens, *Acc. Chem. Res.*, 2013, **46**, 2597–2606.

11 Z.-G. Ye, Y. Bing, J. Gao and A. A. Bokov, *Phys. Rev. B: Condens. Matter Mater. Phys.*, 2003, **67**, 104104.

12 H. Tan, H. Takenaka, C. Xu, W. Duan, I. Grinberg and A. M. Rappe, *Phys. Rev. B*, 2018, **97**, 174101.

13 H. Liu, Y. Ye, X. Zhang, T. Yang, W. Wen and S. Jiang, *J. Mater. Chem. C*, 2022, **10**, 13676.

14 X.-B. Han, C.-Y. Chai, B.-D. Liang, C.-C. Fan and W. Zhang, *CrystEngComm*, 2022, **24**, 1507.

15 Y.-F. Zhang, F.-F. Di, P.-F. Li and R.-X. Xiong, *Chem. – Eur. J.*, 2021, **28**, e202102990.

16 H.-Y. Ye, Y.-Y. Tang, P.-F. Li, W.-Q. Liao, J.-X. Gao, X.-N. Hua, H. Cai, P.-P. Shi, Y.-M. You and R.-G. Xiong, *Science*, 2018, **361**, 151–155.

17 H. Morita, R. Tsunashima, S. Nishihara, K. Inoue, Y. Omura, Y. Suzuki, J. Kawamata, N. Hoshino and T. Akutagawa, *Angew. Chem., Int. Ed.*, 2019, **58**, 9184–9187.

18 Y. Xie, Y. Ai, Y.-L. Zeng, W.-H. He, X.-Q. Huang, D.-W. Fu, J.-X. Gao, X.-G. Chen and Y.-Y. Tang, *J. Am. Chem. Soc.*, 2020, **142**, 12486–12492.

19 A. Katrusiak and M. Szafranski, *Phys. Rev. Lett.*, 1999, **82**, 576.

20 A. Katrusiak, *J. Mol. Struct.*, 2000, **552**, 159–164.

21 M. Szafranski, A. Katrusiak and G. J. McIntyre, *Phys. Rev. Lett.*, 2002, **89**, 215507.

22 S. Horiuchi, Y. Tokunaga, G. Giovannetti, S. Picozzi, H. Itoh, R. Shimano, R. Kumai and Y. Tokura, *Nature*, 2010, **463**, 789–792.

23 S. Horiuchi and S. Ishibashi, *Chem. Sci.*, 2021, **12**, 14198.

24 S. Horiuchi, F. Kagawa, K. Hatahara, K. Kobayashi, R. Kumai, Y. Murakami and Y. Tokura, *Nat. Commun.*, 2012, **3**, 1308.

25 H.-Y. Ye, Y. Zhang, S.-I. Noro, K. Kubo, M. Yoshitake, Z.-Q. Liu, H.-L. Cai, D.-W. Fu, H. Yoshikawa, K. Awaga, R.-G. Xiong and T. Nakamura, *Sci. Rep.*, 2013, **3**, 2249.

26 N. Zhang, Y. Zhang, H.-H. Jiang, G.-W. Du, Q. Pan, R.-G. Xiong and H.-Y. Zhang, *Chem. Mater.*, 2022, **34**, 8077–8086.

27 X.-J. Song, Z.-X. Zhang, X.-G. Chen, H.-Y. Zhang, Q. Pan, J. Yao, Y.-M. You and R.-G. N. Xiong, *J. Am. Chem. Soc.*, 2020, **142**, 9000–9006.

28 M. Szafrański, *J. Phys. Chem. B*, 2009, **113**, 9479–9488.

29 M. Szafrański and A. Katrusiak, *J. Phys. Chem. B*, 2008, **112**, 6779–6785.

30 M. Szafrański, *Cryst. Growth Des.*, 2010, **10**, 4334–4338.

31 Z. Liu, Y. Yuan, Z. Luo, H. Wan, P. Gao, H. Wu, J. Zhuang, J. Zhang, N. Zhang, H. Liu, W. Ren and Z.-G. Ye, *J. Mater. Chem. C*, 2020, **8**, 5795.

32 E. Aksel and J. L. Jones, *Sensors*, 2010, **10**, 1935–1954.

33 L. Zhang, H. Wang, D. Wang, M. Guo, X. Lou and D. Wang, *Adv. Funct. Mater.*, 2020, **30**, 2004641.

34 Y. Liu, H. Aziguli, B. Zhang, W. Xu, W. Lu, J. Bernholc and Q. Wang, *Nature*, 2018, **562**, 96–100.

35 M. Lusi, *Cryst. Growth Des.*, 2018, **18**, 3704–3712.

36 R. Tsunashima, *CrystEngComm*, 2022, **24**, 1309.

37 S. Chen, R. Shang, B.-W. Wang, Z.-M. Wang and S. Gao, *Angew. Chem., Int. Ed.*, 2015, **54**, 11093–11096.

38 P. Zhao, L. Zhang, Z. Meng and Y. Lei, *Adv. Funct. Mater.*, 2022, **32**, 2205092.

39 L. He, P.-P. Shi, M.-M. Zhao, C.-M. Liu, W. Zhang and Q. Ye, *Chem. Mater.*, 2021, **33**, 799–805.

40 H. Xu, W. Guo, Y. Ma, Y. Liu, X. Hu, L. Hua, X. Han, J. Luo Liu and Z. Sun, *Nat. Commun.*, 2022, **13**, 5329.

41 W.-Q. Liao, D. Zhao, Y.-Y. Tang, Y. Zhang, P.-F. Li, P.-P. Shi, X.-G. Chen, Y.-M. You and R.-G. Xiong, *Science*, 2019, **363**, 1206–1210.

42 M. Szafrański, *J. Mater. Chem. C*, 2013, **1**, 7904.

43 W. Nowicki, A. Olejniczak, M. Andrzejewski and A. Katrusiak, *CrystEngComm*, 2012, **14**, 6428–6434.

44 A. Katrusiak, M. Ratajczak-Sitarz and E. Grech, *J. Mol. Struct.*, 1999, **474**, 135–141.